Unified framework for photon dynamics in non-Euclidean polygonal cavities

Yechun Ding,[1] Yongsheng Wang,[1,2] Peng Li,[3] Yaxin Guo,[1] Yanpeng Zhang,[1] Feng Yun,[1,4] Ce Shang,[5,*] Run-Qiu Yang,[6,†] Caigui Jiang,[7,‡] and Feng Li[1,4,§]

[1]*Key Laboratory for Physical Electronics and Devices of the Ministry of Education & Shaanxi Key Lab of Information Photonic Technique, School of Electronic Science and Engineering, Faculty of Electronic and Information Engineering, Xi'an Jiaotong University, Xi'an 710049, China*

[2]*Department of Electrical and Photonics Engineering, Technical University of Denmark, Kongens Lyngby 2800, Denmark*

[3]*Institute of Regenerative and Reconstructive Medicine, Med-X Institute, The First Affiliated Hospital of Xi'an Jiaotong University, Xi'an 710061, China*

[4]*Solid-State Lighting Engineering Research Center, Xi'an Jiaotong University, Xi'an 710049, China*

[5]*Chinese Academy of Sciences, Aerospace Information Research Institute, Beijing 100094, China*

[6]*Center for Joint Quantum Studies and Department of Physics, School of Science, Tianjin University, Yaguan Road 135, Jinnan District, Tianjin 300350, China*

[7]*State Key Laboratory of Human-Machine Hybrid Augmented Intelligence, and Institute of Artificial Intelligence Robotics, Xi'an Jiaotong University, Xi'an 710049, China*

(Received 30 April 2025; revised 3 June 2026; accepted 1 September 2026; published 18 September 2026)

We extend the concept of polygonal resonators to curved spaces through a unified model governed by a joint curvature parameter. This framework uncovers unique dynamics, including dissipative states defined by hyperbolic fixed points that yield phase diagrams in the curvature space. We find that stability transitions across geometric boundaries are characterized by sharp declines in the quality factor, a manifestation of chaotic instability that is overcome in the wave regime, highlighting the wave nature of wave chaos. A key discovery is the symmetry-driven asymptotic behavior in geodesic-sided cavities, revealing a profound connection between physical dynamics and underlying geometry. We also introduce a "non-Euclidean unit circle" as a general shape-invariant platform for optical simulation. These findings provide a robust framework for studying non-Euclidean wave chaos and point to strategies for designing integrated photonics with enhanced degrees of freedom.

DOI: 10.1103/hmxc-ltdl

I. INTRODUCTION

Optical microcavities supporting whispering gallery modes (WGMs) have garnered significant attention as essential components in integrated photonics, owing to their applications in on-chip coherent and quantum light sources [1–5], filters and isolators [6–8], nonlinear optical platforms [9–11], and high-performance sensors [12–15]. The primary advantage of WGM microcavities lies in their high quality factor (Q factor), while unidirectional emission is achieved by introducing slight deformations, creating chaotic tunneling channels [16]. The chaotic photon dynamics has led to the observation of various exotic phenomena and applications, such as broadband momentum coupling [17,18], broadband frequency combs [19,20], and phase-space tailoring [21]. Recently, the investigation of WGM photon dynamics has extended to non-Euclidean spaces, including Möbius strip microlasers [22] and microcavities on surfaces of revolution [23]. This extension offers an additional degree of freedom for light manipulation, revealing emergent physics in higher-dimensional spaces. The influence of space curvature variation on photon dynamics was explored in a face cavity defined on a spherical surface, which demonstrated that positive curvature significantly reduces dissipation in low-periodic modes, leads to enhanced mode coupling, and generates non-Hermitian exceptional points [24]. Furthermore, chaotic modes respond differently to curvature than their regular counterparts, exhibiting distinctively localized hybrid wave packets [25,26].

In addition to the near-circular cavities, polygonal microcavities have been extensively studied for both fundamental physics and practical applications [27–30]. The appeal of polygonal cavities lies in the intrinsic relationship between their geometry and the associated physical phenomena [31,32]. The polygonal shape makes such cavities particularly promising for directional laser emission [27,28] and enables the bottom-up fabrication of micro and nanolasers [33–39]. To increase the Q factor of the pseudointegrable cavities, designs incorporating circular-sided polygons have been proposed to improve the stability of the period modes while simultaneously introducing chaotic dynamics [40]. In this context, it is crucial to understand whether the principles governing

*Contact author: shangce@aircas.ac.cn
†Contact author: aqiu@tju.edu.cn
‡Contact author: cgjiang@xjtu.edu.cn
§Contact author: felix831204@xjtu.edu.cn

polygonal microcavities, featuring both straight and curved sides, can be extended to non-Euclidean space. How would the photon dynamics respond to the curvature of space? Are there fundamental differences between cavities with geodesic and nongeodesic sides? Can Euclidean cavities be regarded as a special case of the non-Euclidean framework? Finally, can the concept of non-Euclidean WGMs be further extended to a broader scope of physics and applications?

In this work, we propose a general model for non-Euclidean polygonal microcavities, where photon dynamics are governed by the interplay between spatial and boundary curvatures—validated in both ray and wave regimes of chaotic photon motion [25]. In the ray chaos regime, such geometric control induces distinct stability transitions between stable and unstable fixed points, giving rise to hyperboliclike loss channels rooted in chaotic instability. Notably, the stability transition boundaries of geodesic cavities exhibit unique asymptotic behaviors consistent with cavity symmetry, highlighting a fundamental distinction from their nongeodesic counterparts. In the wave regime, sharp variations in the quality factor (Q factor) emerge at these stability transition points, in perfect correspondence with the hyperbolic loss channels predicted by ray dynamics. Nevertheless, striking deviations from ray dynamics are also observed as a hallmark of wave chaos, characterized by the suppression of classical chaotic channels due to wavelike uncertainty. We further extend the scope of our model by establishing the concept of a non-Euclidean unit circle—a shape-invariant system with broad implications for optical simulations. Specifically, we demonstrate that this non-Euclidean unit circle enables the simulation of particle or wave packet dynamics in infinitely long periodic potentials using compact single WGM cavities, drastically reducing the size and complexity of the required experimental setups. Our results provide fundamental insights into WGMs in non-Euclidean systems, establish a general framework for shape-invariant optical simulation, and offer strategies for designing photonic devices with enhanced degrees of freedom.

II. THEORETICAL MODEL

We begin with a regular polygonal cavity on a hemispherical surface, as shown in Fig. 1(a). Let R_s denote the radius of curvature of the spherical surface, with O the center of the sphere. The center of the polygonal surface is denoted as O'', and the line connecting O and O'' is taken as the z axis. R_e represents the distance between the vertex A_i ($i = 1, 2, \ldots, N$, where N is the number of sides) and the z axis, which intersects the z axis at O'. To maintain a constant cavity size, we set $R_e = 2$ μm. The effective curvature of space, denoted by η, is defined by $\sin(\eta \times \pi/2) = R_e/R_s$, which is inversely proportional to R_s and confined to $0 < \eta < 1$.

The key challenge is defining the curvature of the sides, since all lines on the spherical surface are curved from a Euclidean perspective. This is addressed by introducing a variable z_m, the length of OC, where C is a point on the segment OO'. The point C and two adjacent vertices form a plane CA_iA_{i+1}, which intersects the spherical surface. The curve of intersection defines the side connecting the ith and $(i+1)$th vertices, as illustrated by the dotted lines in Fig. 1(a). The effective curvature of the side is then defined as $\zeta = z_m/L$, where L is the length of OO'. The variable ζ is constrained to $0 \leqslant \zeta \leqslant 1$, with $0 \leqslant z_m \leqslant L$.

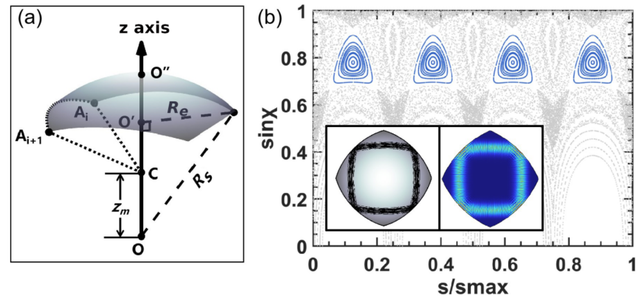

FIG. 1. Theoretical model and photon dynamics of the non-Euclidean polygonal microcavity. (a) Schematic of the microcavity. O and O'' denote the center of the sphere and the polygon, respectively. A_i and A_{i+1} denote the ith and $(i+1)$th vertices of the polygonal cavity, respectively. O' represents the perpendicular foot of the vertex on the z axis, with C being a point along OO'. (b) Poincaré surface of section (PSOS) for a non-Euclidean polygonal microcavity with $\eta = 0.5$ and $\zeta = 0.3$. The blue points correspond to four-periodic motion, while the gray points indicate chaotic trajectories. Insets show light trajectories (left) and optical field (right) for the four-periodic islands.

Together, η and ζ fully describe the cavity geometry and are collectively referred to as the joint curvature $G = (\eta, \zeta)$. As such, the terms "straight" and "curved" should be replaced by "geodesic" and "nongeodesic": A polygon is geodesic (resp. nongeodesic) if its sides are (resp. are not) geodesic lines. When $\zeta = 0$ (i.e., C coincides with O), the sides are great circles—geodesic lines on the spherical surface. They remain geodesic for varying η and become straight lines when $\eta = 0$ (flat space), yielding a Euclidean polygon with straight sides. When $\zeta = 1$ (i.e., C coincides with O'), the curvature of the sides is sufficiently large that the polygon becomes a circle on the spherical surface; this boundary remains circular for varying η and reduces to a Euclidean circle when $\eta = 0$. For intermediate values $0 < \zeta < 1$, the polygon has nongeodesic sides, which reduce to Euclidean polygons with curved sides (Ref. [40]) when $\eta = 0$.

To connect our parametrization to the measurable concept of side curvature, the physical radius of curvature of each side is determined by both parameters:

$$R_c(\eta, \zeta)^2 = R_s(\eta)^2 - \frac{\zeta^2 \cdot L(\eta)^2 \cdot R_e^2}{R_e^2 + 2(1-\zeta)^2 L(\eta)^2}, \tag{1}$$

while η also governs the Gaussian curvature of the three-dimensional polygonal cavities.

As η (resp. ζ) increases, the integrability of the system (excluding polygons with three or four sides) increases, ultimately reaching a value of 1, at which the cavity becomes the surface of a hemisphere (resp. a spherical cap).

III. RAY DYNAMICS AND STABILITY TRANSITION

We consider quadrilateral cavities for simplicity, with the understanding that the results can be extended to polygonal cavities with more sides. The ray trajectories and wave

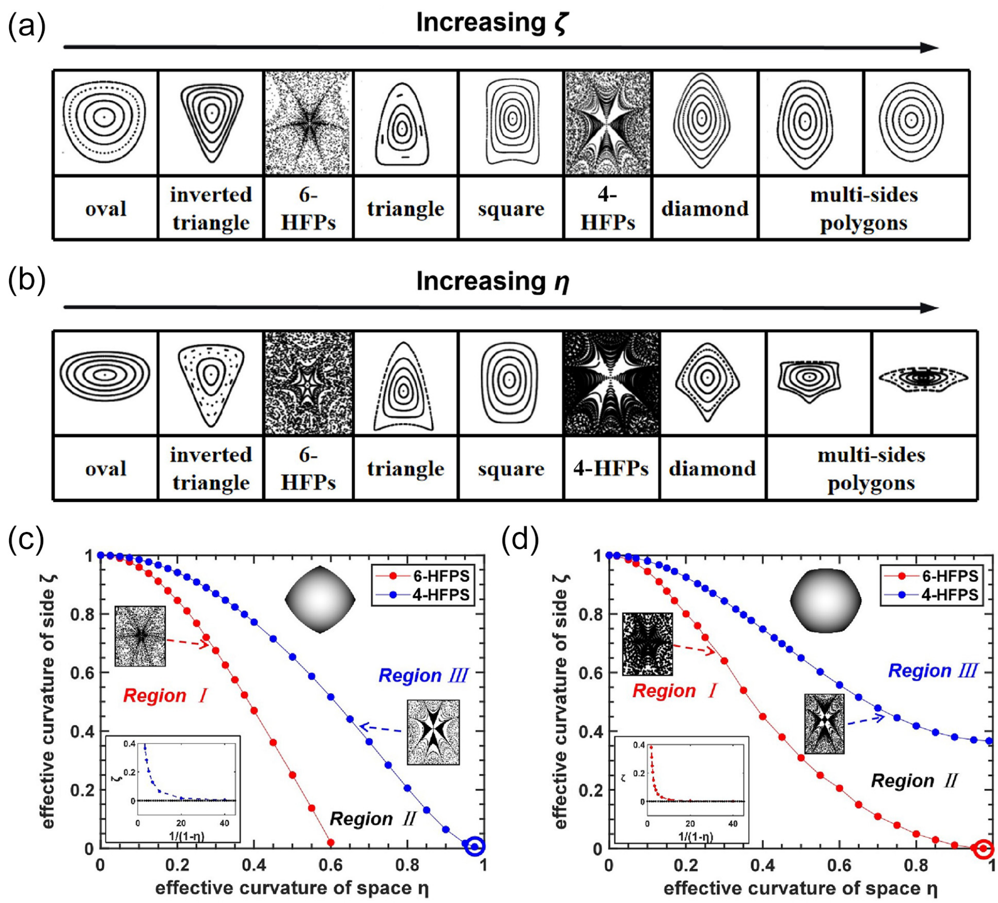

FIG. 2. Island morphology of the non-Euclidean polygonal microcavity under the variation of geometric curvatures. The island shape varies with different geometric parameters while keeping $\eta = 0.3$ [panel (a)] and $\zeta = 0.5$ [panel (b)] as constants, respectively. (c), (d) Phase diagrams for quadrilateral and hexagonal cavities. The six-HFPs (red dashed lines) and four-HFPs (blue dashed lines) partition the phase diagram into three regions: Regions I–III. Insets show the relevant phase-diagram data near (1, 0) with the horizontal axis transformed to $1/(1-\eta)$, where $\eta = 1$ corresponds to the extreme limit of a full hemispherical surface.

distribution for an eigenstate are shown in the insets of Fig. 1(b) for $\eta = 0.5$ and $\zeta = 0.3$ [24,25]. The calculated PSOS is shown in Fig. 1(b), which reveals four-period islands (indicated in blue) surrounded by the chaotic sea. To study the impact of varying the curvature parameters η and ζ, we gradually adjust these parameters and monitor the changes in both the shapes and positions of the islands. As illustrated in Fig. 2(a), the shape of the islands transitions with varying ζ through a series of oval, inverted triangle, triangle, square, diamond, and multisided (with more than four sides) polygons, eventually returning to an oval shape. Throughout this process, the positions of the islands remain at the same height in the PSOS. We refer to these different island shapes as polygonal fixed points (PFPs) in the PSOS. It is important to note that the ovals observed at $\zeta = 0$ and $\zeta = 1$ represent distinctly different features, corresponding to polygonal shapes with two sides ($\zeta = 0$) and an infinite number of sides ($\zeta = 1$), respectively. Additionally, as η increases, a similar variation in the shape of the islands occurs; however, the positions of the islands shift upward, and the shapes become more compressed at higher values of η, as shown in Fig. 2(b). This behavior is a typical effect of the increasing curvature of the space [24]. It is noteworthy that transient states of hyperbolic fixed points (HFPs) appear at the transition between different shapes of PFPs. Specifically, a set of six-branch (resp. four-branch) HFPs occurs at the transition between inverted triangles (resp. squares) and triangles (resp. diamonds). Detailed evolution of the full PSOS is provided in Appendix C. In contrast to PFPs, HFPs represent unstable states that lead to the divergence of photon dynamics into the chaotic sea, thereby reducing the Q factor.

We extend our analysis to polygons with more than four sides and observe the same evolution of island shapes as in quadrilateral cavities (see Appendix C). This indicates the shape transition is a general property of polygonal cavities rather than specifically for quadrilaterals.

To locate the HFPs, we examine the Jacobian matrix J on the Poincaré surface of section. For area-preserving maps, the stability of a fixed point is determined by the trace $\mathrm{Tr}\,J$: elliptic when $|\mathrm{Tr}\,J| < 2$, parabolic when $|\mathrm{Tr}\,J| = 2$, and hyperbolic when $|\mathrm{Tr}\,J| > 2$ (see Appendix A for the formal definition). As the joint curvature $G = (\eta, \zeta)$ varies, $\mathrm{Tr}\,J$ evolves continuously through the following sequence: elliptic $\rightarrow$ parabolic boundary $\rightarrow$ hyperbolic region $\rightarrow$ parabolic boundary $\rightarrow$ elliptic. The two parabolic boundaries enclose a narrow strip where the fixed points are genuinely hyperbolic.

Within this strip, $|\mathrm{Tr}\, J|$ attains a maximum along an interior ridge; it is this ridge that is plotted as the HFP line in the phase diagram in Fig. 2 [41].

By recording the joint geometric parameters $G = (\eta, \zeta)$ at which the fixed point transitions to a hyperbolic state, we construct a two-dimensional (2D) phase diagram, as shown in Fig. 2(c). The red and blue dotted lines, corresponding to the geometric positions of the six-branch and four-branch HFPs (maximal $|\mathrm{Tr}\, J|$), respectively, divide the phase diagram into three regions based on the number of sides of the island polygons: two to three sides in Region I, three to four sides in Region II, and four to infinite sides in Region III. Any stability transition across the HFP lines induces a drop and subsequent recovery of system stability. Importantly, the transition is not abrupt but featured by a gradual evolution of the size and shape of the islands, while the sharp lines in the phase diagram mark the interior ridge of maximal $|\mathrm{Tr}\, J|$ rather than an abrupt boundary. The phase diagrams for polygonal cavities with more sides exhibit similar features, as shown in Fig. 2(d) for hexagonal cavities, while those for the triangle, pentagon, and octagon are presented in Appendix D.

Significant features can be identified by further examining the phase diagrams of various polygonal cavities. We find that the axis defined by $\zeta = 0$ (i.e., the η axis) asymptotically approaches, but never crosses, the six-branch (resp. four-branch) HFP line as η approaches 1 in the hexagonal (resp. quadrilateral) cavity. The HFP is only reached when $\eta = 1$, exhibiting an asymptotic behavior toward the axis $1/(1 - \eta)$ in the insets of Figs. 2(c) and 2(d). It is noteworthy that such an asymptotic behavior occurs exclusively when the geometry of the cavity and the HFPs share the same symmetry—namely, hexagonal versus six-branch and quadrilateral versus four-branch. This phenomenon does not occur in polygons with different symmetries, as illustrated in the phase diagrams shown in Appendix D. Therefore, the asymptotic behavior is a key feature of geodesic polygonal cavities ($\zeta = 0$), reflecting a profound connection between geometric symmetry and physical motion in non-Euclidean spaces. The symmetry-governed asymptotic behavior reported here constitutes a key physical principle that distinguishes geodesic polygons in curved space. While its full analytical derivation remains an open theoretical challenge, this clear empirical law establishes a foundational correspondence between geometry, symmetry, and dynamics—offering a concrete and general framework to guide future studies in non-Euclidean wave chaos and photonics.

IV. WAVE-OPTICAL MANIFESTATIONS OF HYPERBOLIC LOSS CHANNELS

We now consider practical optical devices analyzed using wave optics, which inherently involve wavelike uncertainty and coherence. Consequently, the system can be viewed as an optical platform of wave chaos, as discussed in previous works [25]. For high precision with fine mesh density, we employ the principle of transformation optics to establish an equivalent 2D cavity with a gradient refractive index distribution (details in Appendix E) [42–45] and perform the simulation using COMSOL MULTIPHYSICS (version 5.6) [24,25] (see Appendix H for mesh convergency analysis). The influence of the cavity thickness—an important parameter for practical microcavity devices—is incorporated into the effective refractive index of the two-dimensional model. The calculated Q factors as a function of ζ, η, and resonant frequency are presented in Figs. 3(a) and 3(b). At shorter wavelengths [e.g., azimuthal number $m = 88$ in Fig. 3(a)], distinct valleys emerge, characterized by orders-of-magnitude drops in the Q factor. The minima of these valleys, circled in the plot, correspond directly to the (η, ζ) parameters of the HFPs in the phase diagram of Fig. 2(c). These valleys become shallower as the wavelength increases and are nearly flattened at $m = 36$, as shown in Fig. 3(b). We further analyze these phenomena using Husimi projections onto the PSOS [46,47] in Figs. 3(c)–3(f). In the more "particlelike" regime ($m = 88$), clear loss channels are observed for the HFP, as indicated by the black arrows in Fig. 3(c); these channels are absent for the PFP in Fig. 3(d). A momentum spectral analysis [48], as shown in the insets of Figs. 3(c) and 3(d) and detailed in Appendix B, indicates that the field is more centralized in the PFP with the most central narrow peak carrying 25.18% of the total energy. This value, however, is merely 17.38% for the HFP, which indicates a spreading of energy to the sidebands, resulting in greater light leakage out of the main stable orbits. In contrast, in the more "wavelike" regime [Figs. 3(e) and 3(f)], the wave packets expand beyond the regular island region and the momentum distributions in the insets of Figs. 3(e) and 3(f) show no difference in energy centralization between the PFP and HFP situations. This introduces a major loss mechanism that exceeds the loss from chaotic channels, representing a fascinating optical manifestation of wave chaos: the position-momentum uncertainty of wave mechanics overwhelms the chaotic instability of classical ray mechanics.

V. GEOMETRIC TRANSFORMATION AND THE NON-EUCLIDEAN UNIT CIRCLE

Interestingly, we employ a transformation optics method grounded in differential geometry to make the system shape invariant, namely, to map any non-Euclidean polygonal cavity with parameters (η, ζ) onto a non-Euclidean unit circle. This transformation reveals a rich landscape of optical potential, as detailed in Appendix F. Figure 4(a) shows the result for a quadrilateral cavity with $(\eta, \zeta) = (0.6, 0.59)$. The resulting optical potential can be reasonably fitted by

$$V_{\mathrm{eff}} = -\sum_{i=1}^{4} \frac{M}{|\boldsymbol{r} - \boldsymbol{r}_i|} - \frac{m}{r^4 + q}, \qquad (2)$$

where, r_i denotes the position vector of particles M and m, and q represents the potential softening parameter in the unit circle, as shown in Fig. 4(b). Equation (2) resembles a gravitational-like potential field, except for the r^4 term, which has no counterpart in three-dimensional physical space. By extending this methodology beyond polygonal cavities—focusing instead on the unit circle—we can use a non-Euclidean unit circle to simulate an actual physical field. This approach constitutes a practical method for obtaining solutions to dynamical equations through measurements of non-Euclidean WGM cavities.

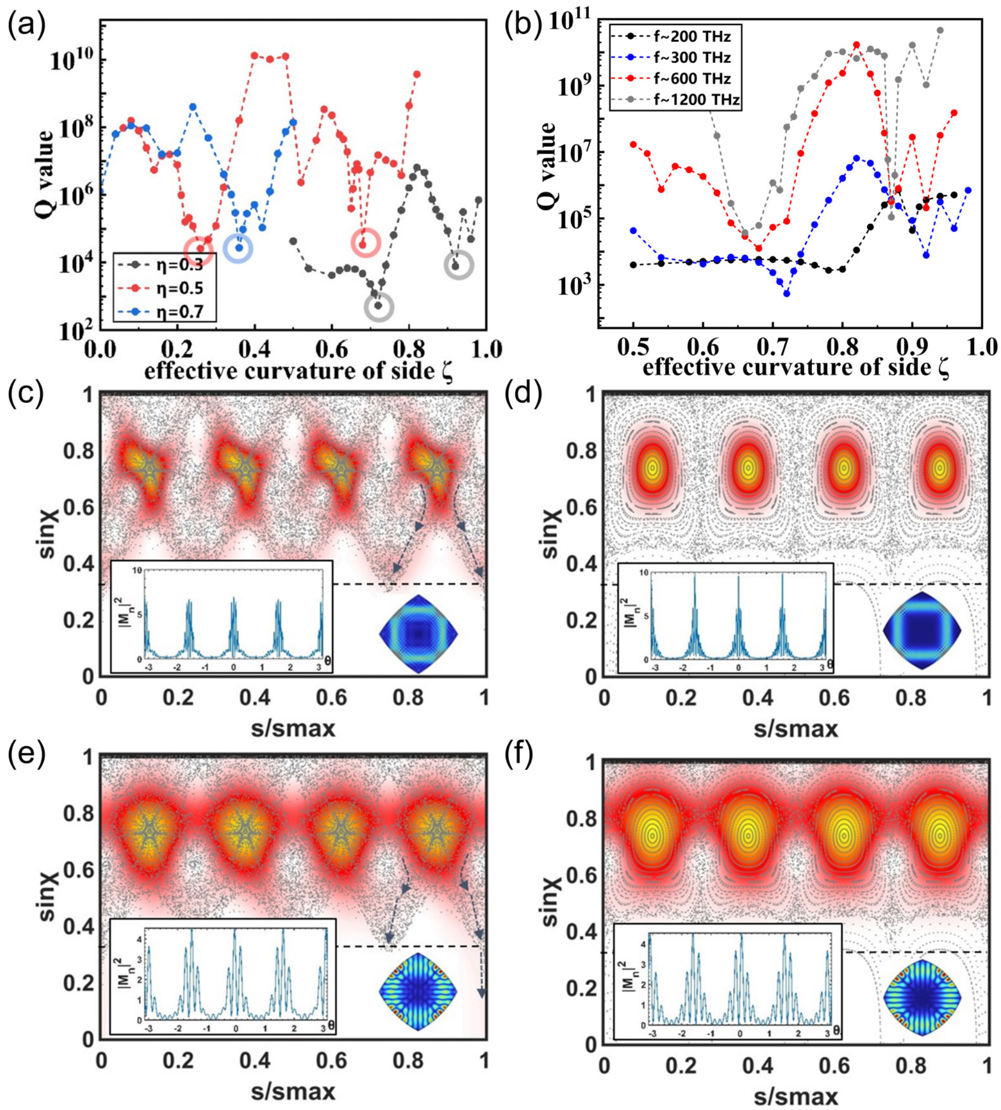

FIG. 3. Analysis of four-periodic motions using wave dynamics. (a) Q factors as a function of ζ for $\eta = 0.3$ (black), 0.5 (red), and 0.7 (blue) within a narrow frequency range around 600 THz (azimuthal number $m = 88$). The valley minima for $\eta = 0.3$, $\eta = 0.5$, and $\eta = 0.7$ are highlighted by black, red, and blue circles, respectively. (b) Q factors as a function of ζ for four different optical frequency ranges (around 1200, 600, 300, and 200 THz, with $m = 188$, 88, 48, and 36), while keeping $\eta = 0.3$. (c)–(f) Husimi projections (red shading) of the four-period island mode for various values of ζ and azimuthal numbers m. (c), (d) $m = 88$; (e), (f) $m = 36$ for HFP and PFP, respectively. The spatial field distributions and the directional integration of momentum distribution of each mode are shown as insets in each graph.

A direct application is to emulate infinite periodic potentials. As shown in Fig. 4(c), when the mirror reflections of rays at the cavity periphery are unfolded, the WGM cavity becomes equivalent to a one-dimensional periodic structure. To demonstrate this transformation for actual periodic structures, we present the equivalent non-Euclidean unit circle for a standard tetragonal lattice in Fig. 4(d) [the original lattice potential is presented in Fig. 4(e)], with other analogous results for hexagonal and triangular lattices provided in Figs. 4(f)–4(i). These transformations are achieved primarily by adjusting the symmetry and the ratio M/m (where M and m are the charges of the field source), as detailed in Appendix G. The non-Euclidean cavity, characterized by nonuniform space curvature in the unit circle, acts as an artificial atom for the optical simulation and experimental design of diverse lattices. A key advantage is its ability to compress a nearly infinite periodic system into a compact ring-shaped orbit with a sufficiently high Q factor. While a detailed comparison with actual periodic lattice systems lies beyond the scope of this work, the mapping itself provides a rigorous geometric foundation for future exploration of compact photonic simulators. Notably, the resulting WGMs exhibit three-, four-, and sixfold rotational symmetries, which differ fundamentally from those of the original lattices—highlighting a profound symmetry transition brought about by the geometric transformation.

VI. CONCLUSION

In conclusion, we extend the concept of polygonal microcavities to non-Euclidean spaces and uncover a series of

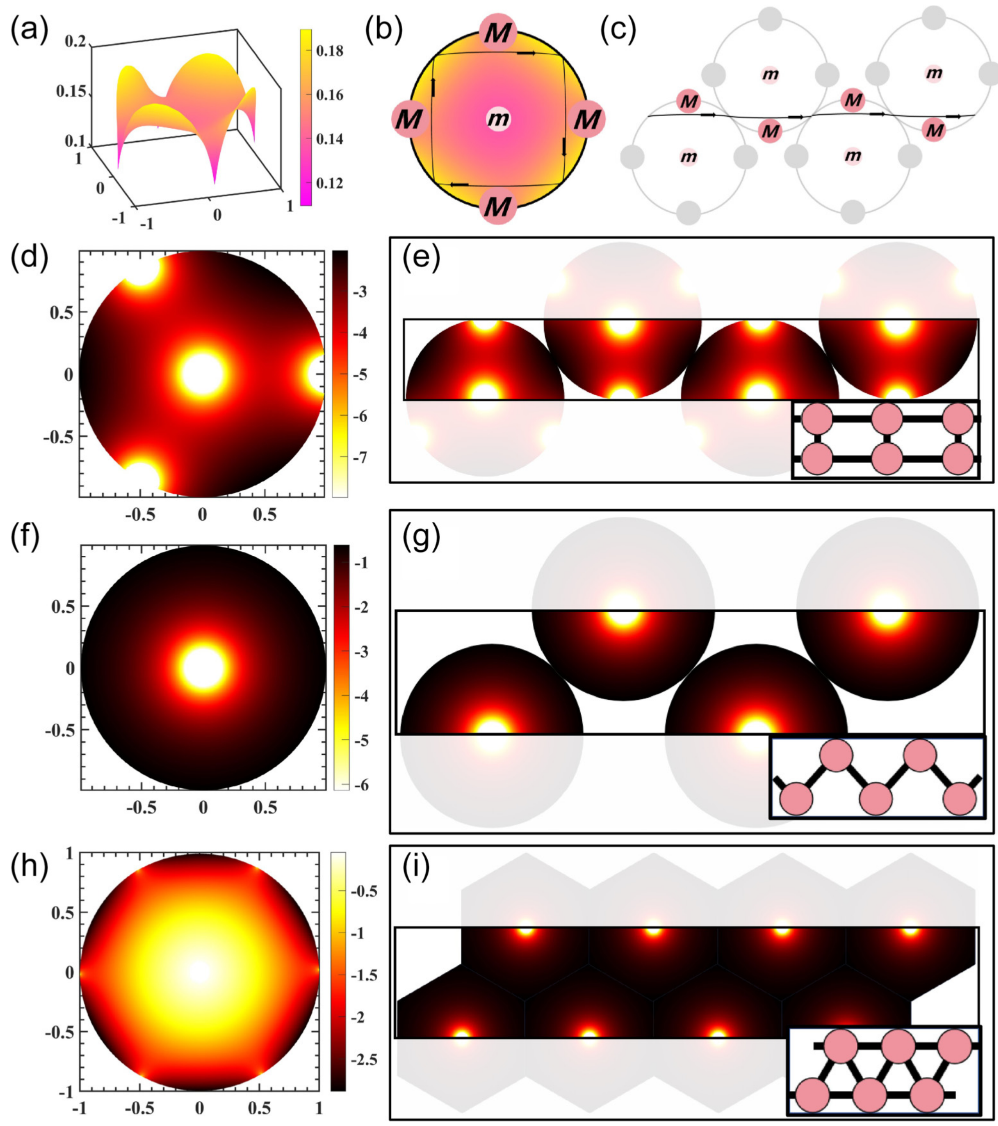

FIG. 4. Simulation of one-dimensional periodic lattice structures via non-Euclidean polygonal microcavities. (a) Three-dimensional potential well diagram illustrating the conformal mapping from spherical quadrilateral microcavities with $G = (0.6, 0.59)$. (b) Schematic representation of the non-Euclidean unit circle for the attractive potential structure. (c) Mirror-unfolded images of gradient refractive index quadrilateral microcavities. By designing potential distributions (d) in the non-Euclidean unit circles, the original tetragonal (e) lattice structures can be obtained after mirror unfolding, where the atomic potential adopts the form of a Yukawa potential modified from the hydrogenlike potential. The insets show the structures of the original lattices. (f), (g) Analogous non-Euclidean unit circle and the corresponding hexagonal lattice. (h), (i) Analogous non-Euclidean unit circle and the corresponding triangular lattice.

consistent physical principles, including the HFP-PFP stability transition, the asymptotic criterion for geodesic cavities, the loss modulation via wave chaos, and the analytical tool of non-Euclidean unit circle. These exotic observations, though manifested under boundary confinement, are direct consequences of the spatial curvature on which the boundaries are defined. Experimental verification can be pursued in microwave systems as well as in hydrodynamic or elastic-wave analogs. The spatially varying effective refractive index representing the curvature can be implemented in practice as a thickness-graded metallic waveguide, which is straightforward to fabricate. For optical realizations, the same index profile can be encoded using a metasurface of subwavelength elements patterned on a planar photonic chip. This paves the way for non-Euclidean cavities to serve as a promising platform for advancing the physics of curved spaces and enables the design of next-generation microlasers and microwave resonators. Specifically, microlasers can be engineered to exhibit local and directional emission by exploiting the dissipation channels of HFPs. Furthermore, ultrahigh-Q polygonal microcavities can be designed by carefully tuning both the boundary and the space curvatures, taking advantage of the multiple degrees of freedom and the precise avoidance of lossy geometries of HFPs. Fundamentally, our system is shown to function as an ideal optical platform for wave chaos and for exploring physical systems with higher-dimensional geometry.

ACKNOWLEDGMENTS

This research was supported by National Key R&D Program of China (Grant No. 2023YFA1407100), the National Natural Science Foundation of China (NSFC) (Grants No. 12474392, No. 12604629, and No. 12074303), the Postdoctoral Fellowship Program of China Postdoctoral Science Foundation (Grant No. GZC20241349), the Tianjin University Self-Innovation Fund Extreme Basic Research Project (Grants No. 2025XJ22-0014 and No. 2025XJ21-0007), and by the Shaanxi Provincial Innovation Capability Support Program No. 2026RC-WZXM-06.

DATA AVAILABILITY

The data that support the findings of this article are not publicly available. The data are available from the authors upon reasonable request.

APPENDIX A: THE ANALYSIS OF JACOBIAN MATRIX

We consider the two-dimensional Poincaré map

$$\mathbf{r}_{n+1} = \mathbf{F}(\mathbf{r}_n), \tag{A1}$$

which describes the dynamics on the phase-space cross section. For Hamiltonian systems, this map is area preserving, and the Jacobian matrix at any point satisfies $\det J(\mathbf{r}) = 1$.

A fixed point $\mathbf{r}^*$ of the map satisfies $\mathbf{r}^* = \mathbf{F}(\mathbf{r}^*)$. Its linear stability is governed by the Jacobian matrix evaluated at $\mathbf{r}^*$,

$$J(\mathbf{r}^*) = \begin{pmatrix} \partial F_x/\partial x & \partial F_x/\partial y \\ \partial F_y/\partial x & \partial F_y/\partial y \end{pmatrix}\Bigg|_{\mathbf{r}=\mathbf{r}^*}. \tag{A2}$$

Since the map is area preserving, the eigenvalues λ_1 and λ_2 of $J(\mathbf{r}^*)$ satisfy $\lambda_1\lambda_2 = \det J = 1$, so they come in reciprocal pairs: $\lambda_2 = 1/\lambda_1$.

The trace of the Jacobian is defined as

$$\mathrm{Tr}[J(\mathbf{r}^*)] = \lambda_1 + \lambda_2. \tag{A3}$$

For area-preserving maps, the stability type of the fixed point is determined solely by the value of the trace relative to ± 2:

(1) If $|\mathrm{Tr}[J(\mathbf{r}^*)]| > 2$, then the eigenvalues are real and satisfy $\lambda_2 = 1/\lambda_1$, with one having magnitude greater than 1 and the other less than 1. The fixed point is a hyperbolic saddle, possessing both stable and unstable manifolds.

(2) If $|\mathrm{Tr}[J(\mathbf{r}^*)]| < 2$, the eigenvalues are complex conjugates lying on the unit circle, i.e., $|\lambda_{1,2}| = 1$. The fixed point is elliptic (neutrally stable).

(3) The marginal cases $\mathrm{Tr}[J(\mathbf{r}^*)] = \pm 2$ correspond to parabolic fixed points, which are nonhyperbolic and require higher-order analysis.

For our polygonal billiard systems, the Jacobian is computed from the linearized reflection and propagation maps along the periodic orbit, and the resulting trace determines whether the orbit is hyperbolic (saddle type) or elliptic.

APPENDIX B: MOMENTUM DISTRIBUTION OF WAVE FUNCTIONS AND THE DIRECTIONAL INTEGRATION

The momentum distribution of wave functions, i.e., their Fourier transforms from coordinate space (x, y) to momentum space (k_x, k_y), provides a useful tool to characterize the changes in a given wave function. The Fourier coefficients $\mathcal{M}_n(k,\theta)$ satisfy

$$\mathcal{M}_n(k,\theta) = \int_\Omega \Psi_n(x,y)e^{-ixk\cos\theta - iyk\sin\theta}\,dxdy, \tag{B1}$$

where $k = \sqrt{k_x^2 + k_y^2}$ and $\theta = \arctan(k_y/k_x)$ are the magnitude and angle of the wave vector, respectively.

The quantity $|\mathcal{M}_n(k,\theta)|^2$ describes the probability weight of the wave function in the plane-wave state with wave vector $(k\cos\theta, k\sin\theta)$. Integrating over all wave vectors with the same direction θ yields the total weight of the wave function propagating along that direction, as shown in Fig. 5.

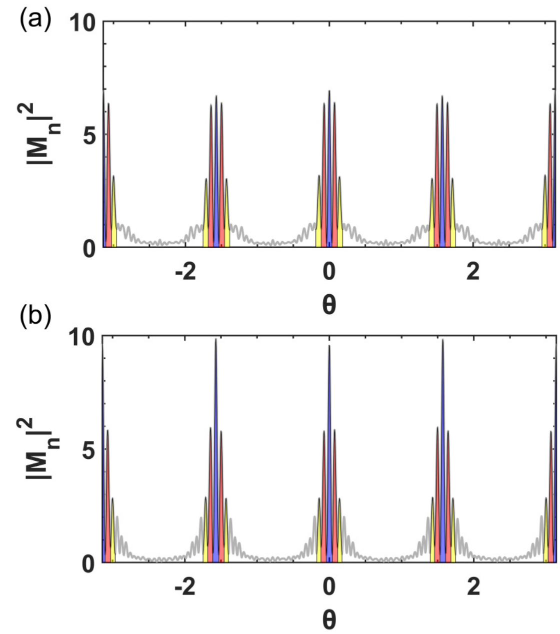

FIG. 5. Directional-integrated momentum-space spectral weight $|M_n|^2$ as a function of angle θ for (a) HFP and (b) PFP optical field configurations. Distinct colored peaks denote the primary (blue), secondary (red), and tertiary (yellow) peaks of spectrum, while gray curves represent the continuous background contribution of the field momentum distribution.

We analyze the momentum distributions and energy ratios of the dominant peaks for the HFP and PFP optical fields based on Fig. 3. The primary (blue), secondary (red), and tertiary (yellow) peaks of the HFP field shown in Fig. 5(a) account for 17.38%, 34.10%, and 17.45% of the total energy, while the corresponding peak fractions of the PFP field in Fig. 5(b) are 25.18%, 30.12%, and 13.51%, respectively. Therefore, it is clear that the field energy is more centralized to the central (primary) peak in the PFP situation while spreads more to sidebands (secondary, tertiary, and more side peaks) in the HFP situation. This difference indicates that the HFP regime features an enhanced contribution of quasiperiodic motion and intensified energy dissipation.

APPENDIX C: FULL PSOS OF QUADRILATERAL AND HEXAGONAL CAVITIES

We present the evolution of the shapes of the polygonal islands with the joint geometry curvatures, as shown in

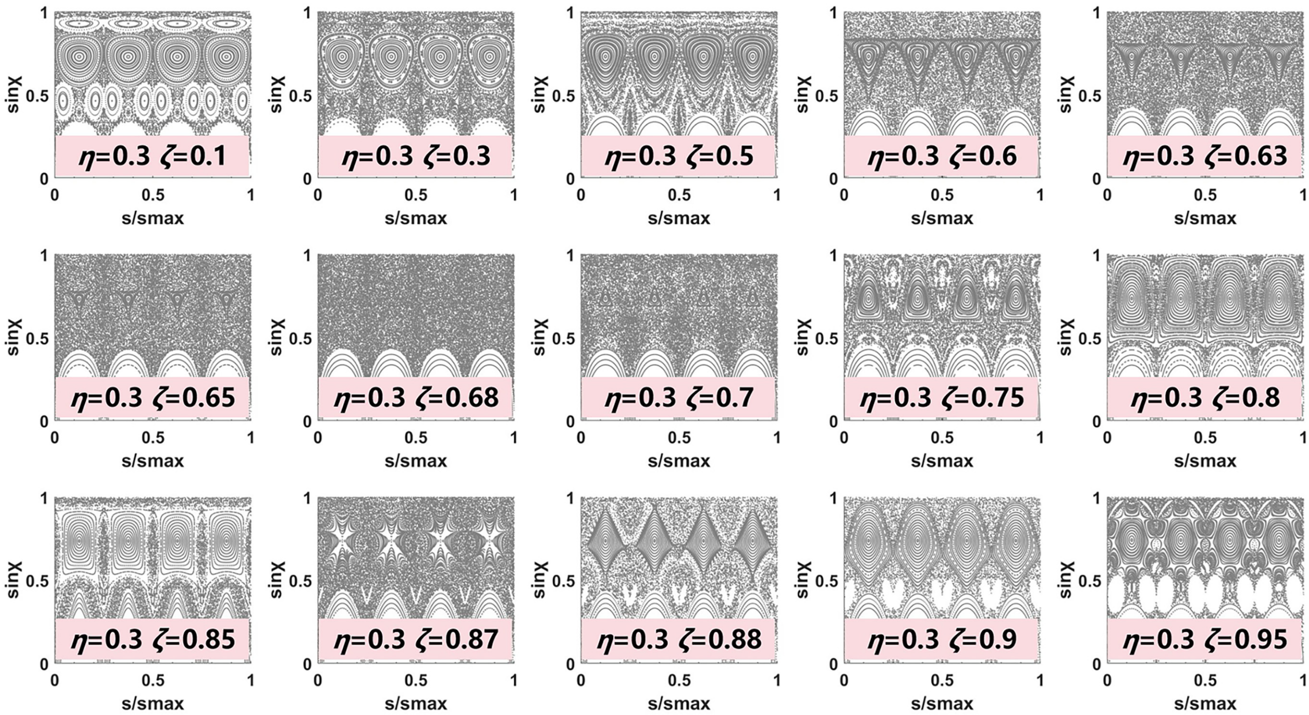

FIG. 6. The full PSOSs of quadrilateral cavities when keeping $\eta = 0.3$ and varying ζ as 0.1, 0.3, 0.5, 0.6, 0.63, 0.65, 0.68, 0.7, 0.75, 0.8, 0.85, 0.87, 0.88, 0.9, and 0.95.

Figs. 6 and 7 for quadrilateral and Figs. 8 and 9 for hexagonal cavities. It is evident that the shape of the islands transitions with varying ζ (η) through a series of oval, inverted triangle, six-branch hyperbolic, triangle, square, four-branch hyperbolic, diamond, and multisided (with more than four sides) polygons, eventually returning to an oval shape.

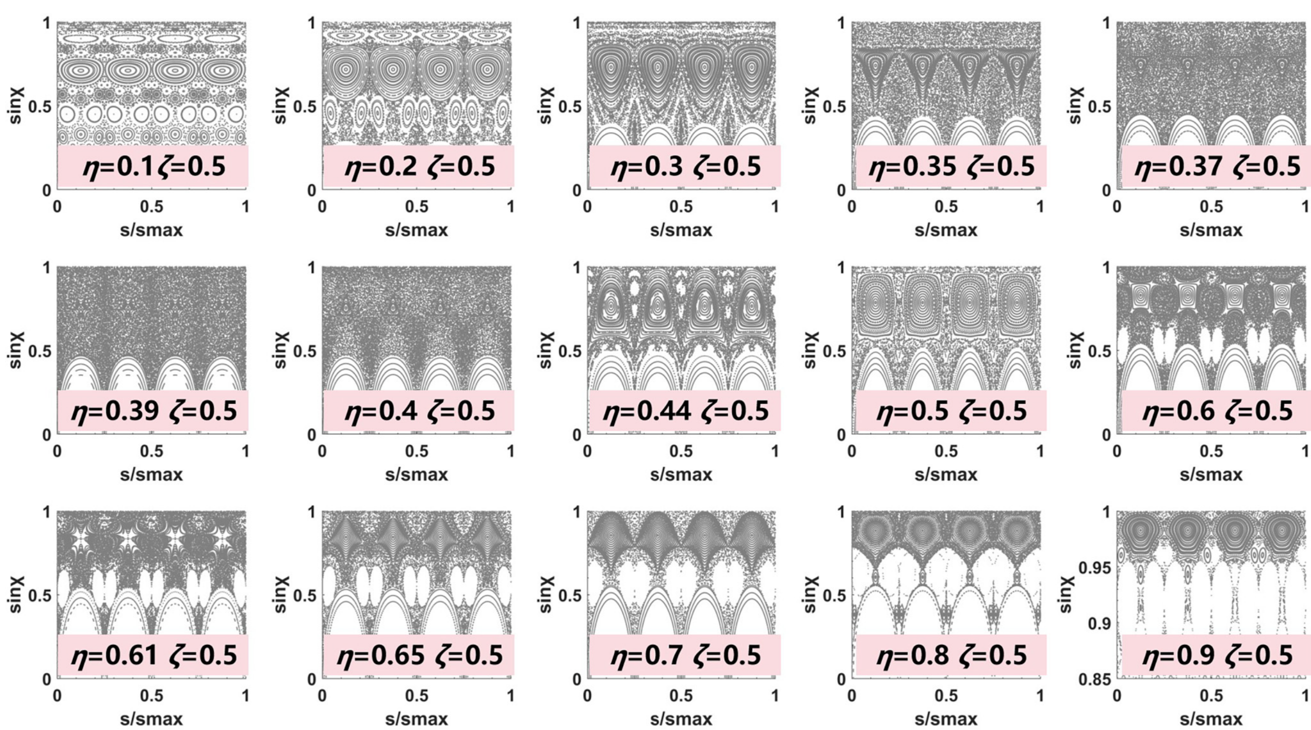

FIG. 7. The full PSOSs of quadrilateral cavities when keeping $\zeta = 0.3$ and varying η as 0.1, 0.2, 0.3, 0.35, 0.37, 0.39, 0.4, 0.44, 0.5, 0.6, 0.61, 0.65, 0.7, 0.8, and 0.9.

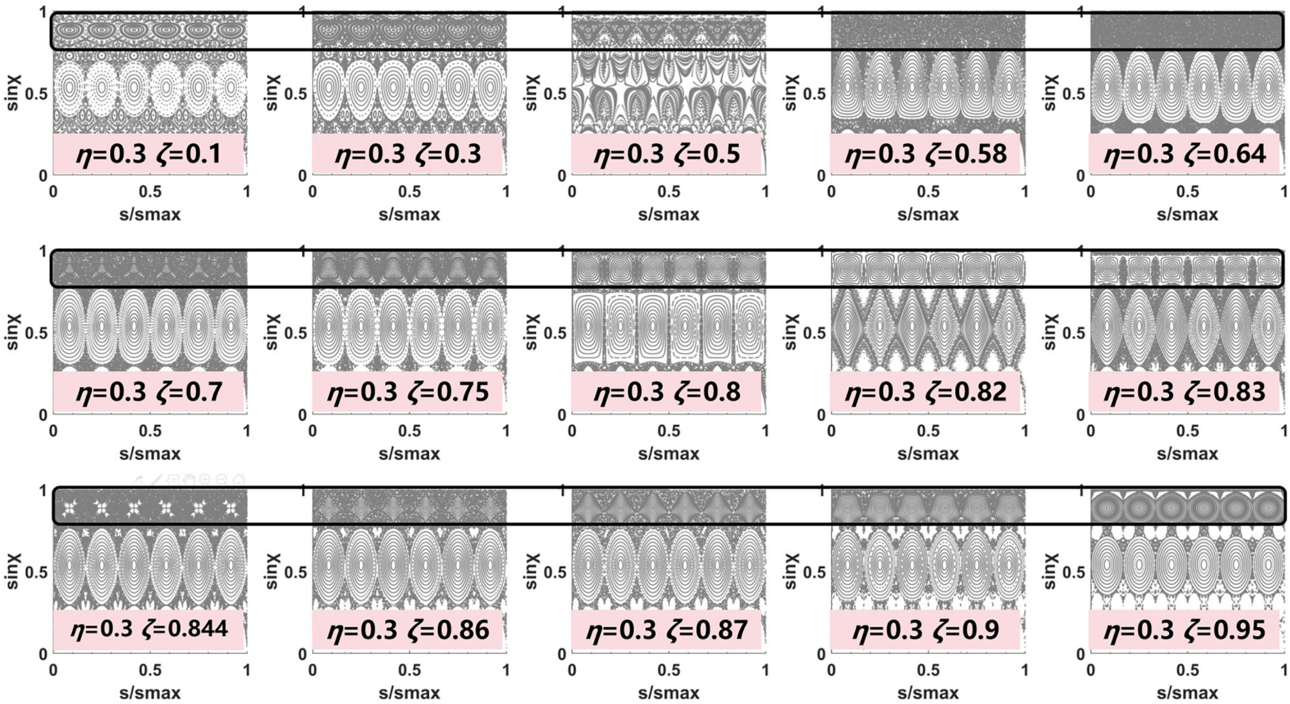

FIG. 8. The full PSOSs of hexagonal cavities when keeping $\eta = 0.3$ and varying ζ as 0.1, 0.3, 0.5, 0.58, 0.64, 0.7, 0.75, 0.8, 0.82, 0.83, 0.844, 0.86, 0.87, 0.9, and 0.95. The six-period motion is enclosed in black rectangular boxes in the PSOSs.

APPENDIX D: THE PHASE DIAGRAM OF FIXED POINTS FOR POLYGONS WITH VARIOUS NUMBERS OF SIDES

We present the phase diagram of fixed points for triangular, quadrilateral, pentagonal, hexagonal, and octagonal cavities, as shown in Fig. 10. It is demonstrated that the blue dashed line, representing the four-branch hyperbolic fixed point, asymptotes to the lower right corner of the phase diagram for quadrilateral cavities, while the red dashed line, representing the six-branch hyperbolic fixed point, asymptotes to the lower right corner of the phase diagram for hexagonal cavities.

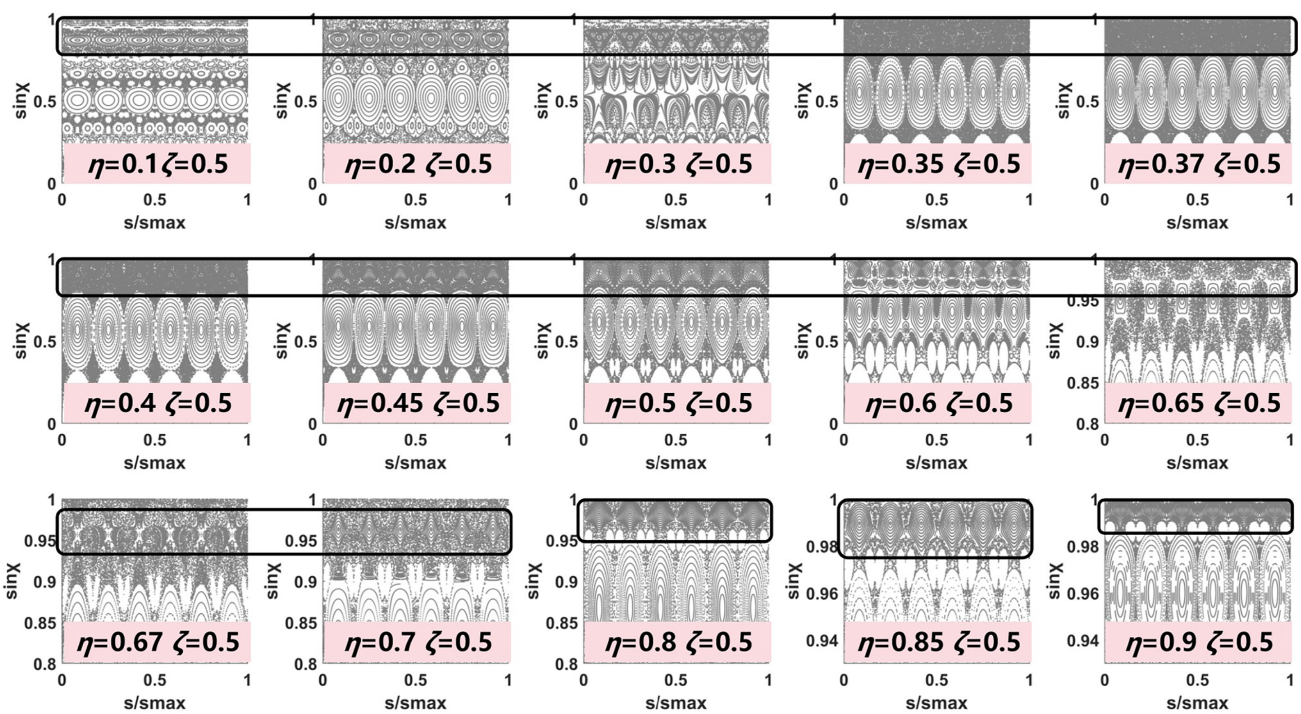

FIG. 9. The full PSOSs of hexagonal cavities when keeping $\zeta = 0.5$ and varying η as 0.1, 0.2, 0.3, 0.35, 0.37, 0.4, 0.45, 0.5, 0.6, 0.65, 0.67, 0.7, 0.8, 0.85, and 0.9 The six-period motion is enclosed in black rectangular boxes in the PSOSs.

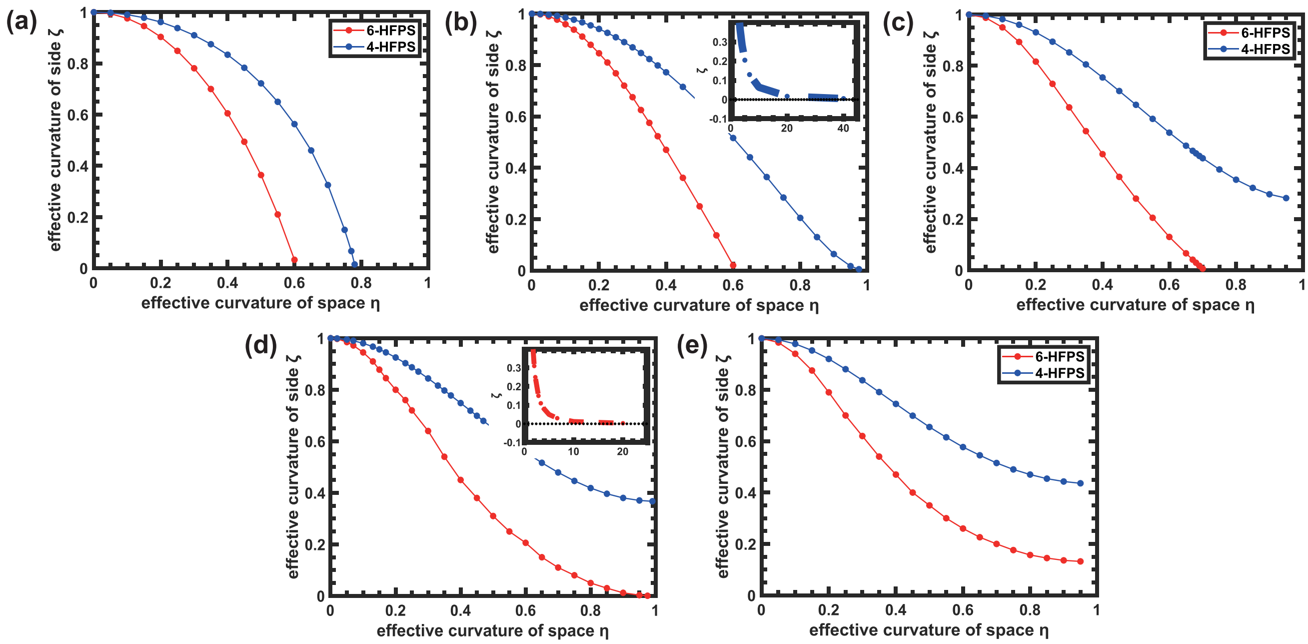

FIG. 10. Phase diagrams for triangular, quadrilateral, pentagonal, hexagonal, and octagonal cavities. The red dashed lines represent six-HFPs, and the blue dashed lines represent four-HFPs. (The phase-diagram curves of the quadrilateral microcavity and hexagonal microcavity asymptoting to the phase point ($\eta = 1$, $\zeta = 0$) are marked by blue and red circles, respectively.) Insets: Asymptotic behavior of $1/(1-\eta)$ vs ζ near $\eta = 1$ and $\zeta = 0$.

APPENDIX E: THE MATHEMATICS OF TRANSFORMATION OPTICS FROM 3D CURVED POLYGONAL CAVITIES TO 2D POLYGONAL CAVITIES

To preserve the invariance of the geodesic equation and the wave equation, it is necessary to perform a transformation from 3D cavities with a uniform refractive index to 2D cavities with a gradient refractive index, such that the conditions of conformal mapping are satisfied. Specifically, this requires that

$$n_{2D}^2(\boldsymbol{r})\, ds_{2D}^2 = n_{3D}^2\, ds_{3D}^2, \tag{E1}$$

where ds_{3D}^2 and ds_{2D}^2 are the line elements of 3D and 2D microcavities, respectively. And for a 3D hemispherical polygonal microcavity, we can use spherical coordinates to present

$$ds_{2D}^2 = R_0^2(d\theta^2 + \sin^2\theta\, d\phi^2), \tag{E2}$$

where R_0 is the spherical radius, ϕ is the rotation angle, and θ is the elevation of the sphere. For a 2D polygonal microcavity, we can use polar coordinates to present

$$ds_{2D}^2 = dr^2 + r^2 d\phi^2, \tag{E3}$$

where r is the polar diameter and ϕ is the polar angle. Thus, by inserting Eqs. (E2) and (E3) into Eq. (E1), we can get

$$\tilde{n}^2(dr^2 + r^2 d\phi^2) = R_0^2(d\theta^2 + \sin^2\theta\, d\phi^2), \tag{E4}$$

where $\tilde{n} = n_{2D}/n_{3D}$, and it is obvious that ϕ in 2D cavity and ϕ in 3D cavity represent the same physical quantity; thus, we can know that

$$\tilde{n} dr = R_0 d\theta, \tag{E5}$$

$$\tilde{n} r = R_0 \sin\theta. \tag{E6}$$

By combining Eqs. (E5) and (E6), we get the relation between polar diameter r in 2D and elevation of the hemispherical cavity θ,

$$r = C \times \tan\left(\frac{\theta}{2}\right). \tag{E7}$$

By inserting Eq. (E7) into Eq. (E6), we can get

$$n_{2D} = n_{3D} \times \frac{2 \times \frac{R_0}{C}}{\left(\frac{r}{C}\right)^2 + 1}. \tag{E8}$$

In this work, we require that the size of the cavities remains unchanged under the geometric transformation; therefore, we

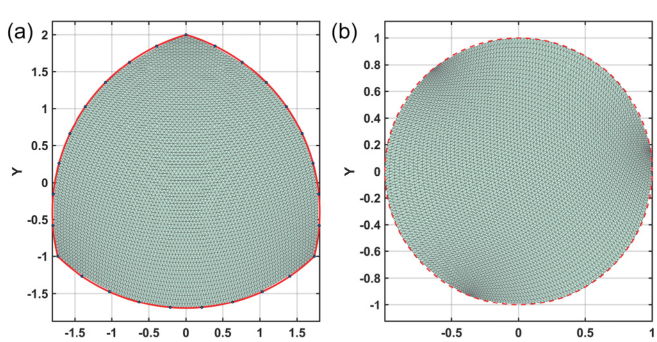

FIG. 11. (a) A curved-edge triangular mesh domain composed of three circular arcs with a radius of curvature equal to 3. (b) A new unit-circle mesh domain obtained by performing the Schwarz-Christoffel mapping on the mesh in panel (a).

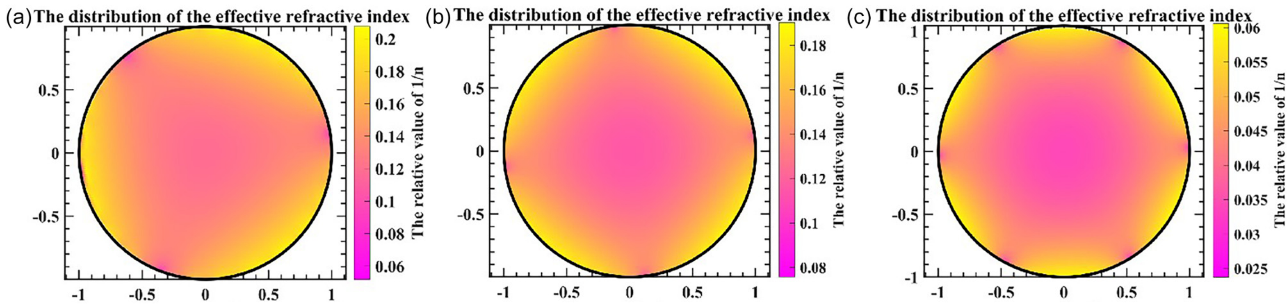

FIG. 12. The refractive index distribution diagrams of unit-circle cavities obtained by conformal mapping of non-Euclidean uniform-refractive-index (a) triangular cavity, (b) quadrilateral cavity, (c) and hexagonal cavity.

keep $R_e = R_0 \sin(\eta \cdot \pi/2)$ as a constant. Thus, when $\theta_{\max} = \eta \cdot \pi/2$, let $r = R_e$; then, we can know

$$C = R_e \tan(\eta \times \pi/4). \tag{E9}$$

The validity of this technique has been rigorously demonstrated in numerous 3D objects, including curved cavities [42–45].

APPENDIX F: THE MATHEMATICS OF TRANSFORMATION OPTICS FROM PLANAR POLYGONAL CAVITIES TO UNIT CIRCLE CAVITIES

We know that Eq. (E1) is the necessary relation that conforms to the physical principle for a conformal mapping. Therefore, we can use the Schwarz-Christoffel mapping—a type of conformal mapping that can map polygonal regions in

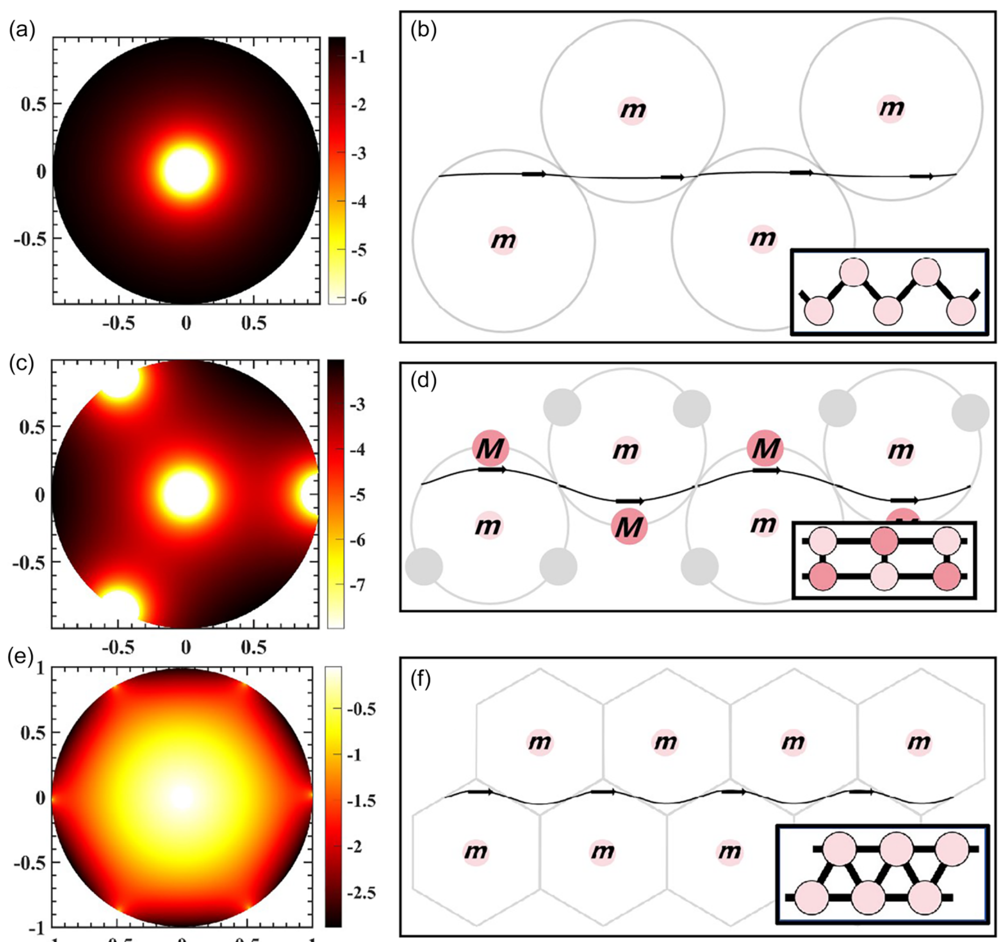

FIG. 13. By designing different potential distributions [panels (a), (c), and (e)] in the non-Euclidean unit circles, the original trigonal, tetragonal, and hexagonal lattice structures can be obtained, respectively, after mirror unfolding. Three different kinds of one-dimensional periodic lattice structures, respectively. (b) Trigonal lattice structure from unit-circle mapping of isotropic non-Euclidean microcavities, (d) tetragonal lattice structure from unit-circle mapping of non-Euclidean triangular microcavities, and (f) hexagonal lattice structure from planar mapping of non-Euclidean hexagonal microcavities.

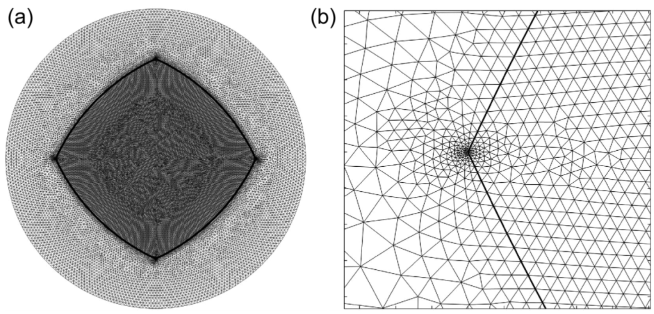

FIG. 14. The overall mesh distribution of the polygonal microcavity and ambient air [panel (a)], and refined meshes at the corner regions of the cavity [panel (b)] in COMSOL modeling.

the complex plane to simple regions such as the unit disk and the upper half plane, and vice versa—to conformally map a planar polygonal region with a gradient refractive index to a unit-circle region with a more complex distribution, where the mapping satisfies the following mathematical relation:

$$f(\zeta)=\int^{\zeta}\frac{K}{(w-a)^{1-(\alpha/\pi)}(w-b)^{1-(\beta/\pi)}(w-c)^{1-(\gamma/\pi)}\dots}dw. \tag{F1}$$

Here, f denotes an analytic conformal mapping from the upper half plane $\{\zeta \in \mathbb{C} : \mathrm{Im}(\zeta) > 0\}$ to the interior of the polygon. This function maps the real axis to the edges of the polygon, where α, β, and γ are the interior angles of the polygon. $a < b < c$ are values of points on the real axis of the ζ plane, corresponding to the vertices of the polygon in the z plane, and K is a complex constant controlling scaling and rotation. Based on the above mathematical foundation, we discretize the boundary and interior of the two-dimensional planar curved-edge polygon into a number of lattice points (specifically, the mapping of the curved-edge triangular cavity), and then perform the Schwarz-Christoffel mapping to obtain the lattice point diagram of the unit circle, as shown in Fig. 11.

According to the relation in Eq. (E1), we need to ensure that the product of the refractive index and the line element remains unchanged before and after the transformation. Therefore, we calculate the product of the average distance between a specified lattice point and its neighboring lattice points, and the refractive index at that point [satisfying Eq. (E8)], to obtain the product of the average distance after mapping and the new refractive index. After recording the new refractive index values of all lattice points, the refractive index distribution map of the unit circle can be obtained, as shown in Fig. 12.

APPENDIX G: DESIGN OF POTENTIAL DISTRIBUTION ON THE UNIT CIRCLE CAVITIES TO SIMULATE PERIODIC LATTICE STRUCTURES

As shown in Figs. 13(b), 13(d), and 13(f), we can perform a mirror reflection along the tangent to the cavity edge at each reflection point of the classical ray trajectory in the island mode of a microcavity supporting WGMs. This operation yields a "cavity chain." Meanwhile, based on the potential well approximation proposed in Eq. (E1) of the original paper, the potential field inside the cavity can be regarded as generated by "atomlike" centers located at positions M and m. Therefore, when we conduct mirror expansions for three types of cavities—(1) a unit circle with a central potential, (2) a unit circle derived from a curved-edge triangle with a central potential via the conformal mapping described in Sec. IV, and (3) a regular hexagon with a central potential—we can obtain one-dimensional periodic lattice structures with trigonal, tetragonal, and hexagonal symmetries, respectively, as shown in Figs. 13(a)–13(f). This approximation is valid due to the short-range nature of the attractive potential, allowing us to only consider the attractive potentials of "atomlike" centers near the ray trajectories of the "cavity chain." When adopting the hydrogenlike Yukawa potential to simulate the atomic potential field, for the trigonal and tetragonal structures, we only need to ensure that the potential distribution at positions M and m in the unit circle satisfies the same relation:

$$V(r) = -\frac{Z}{\rho}e^{-\lambda\rho}, \tag{G1}$$

where Z denotes the nuclear charge number of the hydrogenlike atom, $\rho = r/a_0$ (with a_0 being the Bohr radius) is the dimensionless radial distance, and $\lambda = \mu a_0$ (where μ represents the characteristic decay length) is the dimensionless decay coefficient. Since our focus is on the potential energy distribution in a unit-circle microcavity system with a fixed radius, which is irrelevant to the absolute magnitude of the potential energy, we set $Z = 1/a_0$. Based on its physical significance and the cavity size, μ can be assigned a dimensionless value of 0.5.

Thereby, the unit-circle potential distribution diagrams corresponding to the trigonal and hexagonal lattices can be obtained, as shown in Figs. 13(a) and 13(b). For the hexagonal lattice structure, however, we first introduce the central potential distribution described by Eq. (G1) into the regular hexagonal cavity, and then perform the aforementioned conformal mapping to obtain the unit-circle potential distribution that can simulate the one-dimensional hexagonal lattice structure, as shown in Fig. 13(c).

APPENDIX H: CONVERGENCE AND MESH-SENSITIVITY ANALYSIS OF COMSOL CAVITY MODEL

To guarantee the numerical accuracy of the COMSOL simulations, the distribution and density of computational meshes must be carefully optimized. A mesh scaling parameter N_{mesh} is defined to quantify the mesh resolution, where the maximum and minimum mesh element sizes are set to $d_{\max} = c/(n_{\max} f N_{\mathrm{mesh}})$ and $d_{\min} = d_{\max}/10$, respectively. Here, $n_{\max}$ denotes the maximum refractive index within the two-dimensional polygonal cavity, and f denotes the mode frequency. As shown in Fig. 14(a), meshes are automatically generated in COMSOL using the above parameters, with refined meshes implemented at the corner regions, as displayed in Fig. 14(b).

Furthermore, the value of N_{mesh} is determined via systematic mesh convergence analysis. A typical HFP mode with an eigenfrequency near $f = 600$ THz is selected to investigate the variations in eigenfrequency and logarithmic Q value with increasing N_{mesh}. Convergence is achieved when the relative

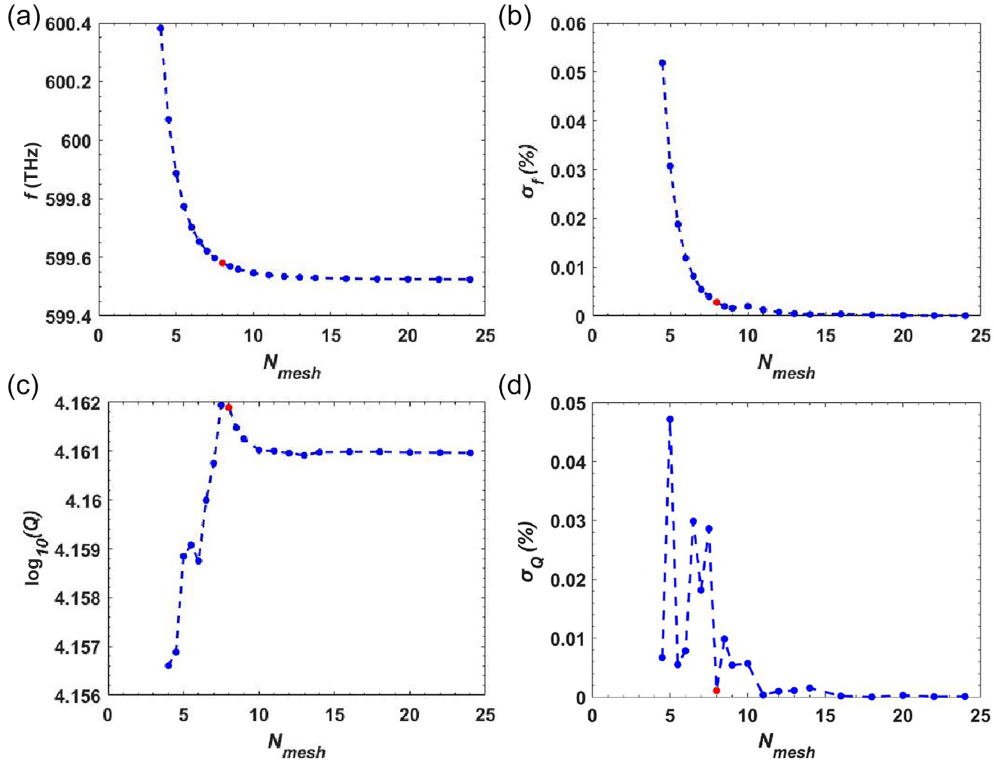

FIG. 15. Convergence and mesh-sensitivity analysis of HFP modes. The grid size parameter n_{mesh} is plotted against (a) the eigenfrequency f, (b) the relative change rate of eigenfrequency σ_f, (c) the logarithm of the quality factor $\log_{10}(Q)$, and (d) the relative change rate of Q values σ_Q. The red marker indicates the value of n_{mesh} selected for the final simulation.

change rates of both quantities are lower than 0.01%, as validated in Fig. 15. Consequently, we adopt $N_{\mathrm{mesh}} = 8$ for all simulations, which balances numerical accuracy and computational cost.

[1] H. J. Kimble, The quantum internet, Nature (London) **453**, 1023 (2008).

[2] P. Lodahl, S. Mahmoodian, S. Stobbe, A. Rauschenbeutel, P. Schneeweiss, J. Volz, H. Pichler, and P. Zoller, Chiral quantum optics, Nature (London) **541**, 473 (2017).

[3] T. J. Kippenberg, A. L. Gaeta, M. Lipson, and M. L. Gorodetsky, Dissipative Kerr solitons in optical microresonators, Science **361**, eaan8083 (2018).

[4] H. Deng, G. L. Lippi, J. Mørk, J. Wiersig, and S. Reitzenstein, Physics and applications of high-β micro- and nanolasers, Adv. Opt. Mater. **9**, 2100415 (2021).

[5] Q. Xu, B. Schmidt, S. Pradhan, and M. Lipson, Micrometre-scale silicon electro-optic modulator, Nature (London) **435**, 325 (2005).

[6] L. Chang, X. Jiang, S. Hua, C. Yang, J. Wen, L. Jiang, G. Li, G. Wang, and M. Xiao, Parity–time symmetry and variable optical isolation in active–passive-coupled microresonators, Nat. Photon. **8**, 524 (2014).

[7] S. Hua, J. Wen, X. Jiang, Q. Hua, L. Jiang, and M. Xiao, Demonstration of a chip-based optical isolator with parametric amplification, Nat. Commun. **7**, 13657 (2016).

[8] Z. Shen, Y.-L. Zhang, Y. Chen, C.-L. Zou, Y.-F. Xiao, X.-B. Zou, F.-W. Sun, G.-C. Guo, and C.-H. Dong, Experimental realization of optomechanically induced non-reciprocity, Nat. Photon. **10**, 657 (2016).

[9] T. Harayama and S. Shinohara, Two-dimensional microcavity lasers, Laser Photonics Rev. **5**, 247 (2011).

[10] T. J. Kippenberg, R. Holzwarth, and S. A. Diddams, Microresonator-based optical frequency combs, Science **332**, 555 (2011).

[11] X.-F. Jiang, Y.-F. Xiao, Q.-F. Yang, L. Shao, W. R. Clements, and Q. Gong, Free-space coupled, ultralow-threshold Raman lasing from a silica microcavity, Appl. Phys. Lett. **103**, 101102 (2013).

[12] X. Xu, W. Chen, G. Zhao, Y. Li, C. Lu, and L. Yang, Wireless whispering-gallery-mode sensor for thermal sensing and aerial mapping, Light: Sci. Appl. **7**, 62 (2018).

[13] A. Schweinsberg, S. Hocdé, N. N. Lepeshkin, R. W. Boyd, C. Chase, and J. E. Fajardo, An environmental sensor based on an integrated optical whispering gallery mode disk resonator, Sens. Actuators B: Chem. **123**, 727 (2007).

[14] N. Toropov, G. Cabello, M. P. Serrano, R. R. Gutha, M. Rafti, and F. Vollmer, Review of biosensing with whispering-gallery mode lasers, Light: Sci. Appl. **10**, 42 (2021).

[15] X. Cao, H. Yang, Z.-L. Wu, and B.-B. Li, Ultrasound sensing with optical microcavities, Light: Sci. Appl. **13**, 159 (2024).

[16] L.-K. Chen, Y.-Z. Gu, Q.-T. Cao, Q. Gong, J. Wiersig, and Y.-F. Xiao, Regular-orbit-engineered chaotic photon transport in mixed phase space, Phys. Rev. Lett. **123**, 173903 (2019).

[17] X. Jiang, L. Shao, S.-X. Zhang, X. Yi, J. Wiersig, L. Wang, Q. Gong, M. Lončar, L. Yang, and Y.-F. Xiao, Chaos-assisted broadband momentum transformation in optical microresonators, Science **358**, 344 (2017).

[18] H. Wang and J. Nöcke, Chaotic ray dynamics enables photonics with broadband light, Sci. China Phys. Mech. Astron. **61**, 014231 (2018).

[19] H.-J. Chen, Q.-X. Ji, H. Wang, Q.-F. Yang, Q.-T. Cao, Q. Gong, X. Yi, and Y.-F. Xiao, Chaos-assisted two-octave-spanning microcombs, Nat. Commun. **11**, 2336 (2020).

[20] W. Wang, L. Wang, and W. Zhang, Advances in soliton microcomb generation, Adv. Photonics **2**, 034001 (2020).

[21] Y.-J. Qian, H. Liu, Q.-T. Cao, J. Kullig, K. Rong, C.-W. Qiu, J. Wiersig, Q. Gong, J. Chen, and Y.-F. Xiao, Regulated photon transport in chaotic microcavities by tailoring phase space, Phys. Rev. Lett. **127**, 273902 (2021).

[22] Y. Song, Y. Monceaux, S. Bittner, K. Chao, H. M. R. de la Cruz, C. Lafargue, D. Decanini, B. Dietz, J. Zyss, A. Grigis, *et al.*, Möbius strip microlasers: A testbed for non-Euclidean photonics, Phys. Rev. Lett. **127**, 203901 (2021).

[23] C. Xu, I. Dana, L.-G. Wang, and P. Sebbah, Light chaotic dynamics in the transformation from curved to flat surfaces, Proc. Natl. Acad. Sci. USA **119**, e2112052119 (2022).

[24] Y. Wang, Y. Ren, X. Luo, B. Li, Z. Chen, Z. Liu, F. Liu, Y. Cai, Y. Zhang, J. Liu, *et al.*, Manipulating cavity photon dynamics by topologically curved space, Light: Sci. Appl. **11**, 308 (2022).

[25] W. Lin, Y. Ding, Y. Wang, P. Li, Y. Zhang, F. Yun, and F. Li, Tailoring chaotic motion of microcavity photons in ray and wave dynamics by tuning the curvature of space, Sci. China Phys. Mech. Astron. **67**, 274214 (2024).

[26] H.-J. Stöckmann, Signatures of non-Euclidean metrics in the optical features of microcavities, Sci. China Phys. Mech. Astron. **68**, 244231 (2025).

[27] J. D. Lin, Y. Z. Huang, Y. D. Yang, Q. F. Yao, X. M. Lv, J. L. Xiao, and Y. Du, Single transverse whispering-gallery mode AlGaInAs/InP hexagonal resonator microlasers, IEEE Photonics J. **3**, 756 (2011).

[28] Y.-D. Yang, M. Tang, F.-L. Wang, Z.-X. Xiao, J.-L. Xiao, and Y.-Z. Huang, Whispering-gallery mode hexagonal micro-/nanocavity lasers [Invited], Photonics Res. **7**, 594 (2019).

[29] D. J. Gargas, M. C. Moore, A. Ni, S.-W. Chang, Z. Zhang, S.-L. Chuang, and P. Yang, Whispering gallery mode lasing from zinc oxide hexagonal nanodisks, ACS Nano **4**, 3270 (2010).

[30] H. Cao and J. Wiersig, Dielectric microcavities: Model systems for wave chaos and non-Hermitian physics, Rev. Mod. Phys. **87**, 61 (2015).

[31] J. Wiersig, Hexagonal dielectric resonators and microcrystal lasers, Phys. Rev. A **67**, 023807 (2003).

[32] X. Luo, Y. Cai, Y. Wang, Z. Chen, F. Liu, L. Zhang, Y. Zhang, and F. Li, Fully deterministic analysis on photonic whispering-gallery modes of irregular polygonal microcavities with testing in hexagons, Phys. Rev. A **103**, L031503 (2021).

[33] Q. Zhang, S. T. Ha, X. Liu, T. C. Sum, and Q. Xiong, Room-temperature near-infrared high-Q perovskite whispering-gallery planar nanolasers, Nano Lett. **14**, 5995 (2014).

[34] A. Feng, X. Jiang, X. Zhang, X. Zheng, W. Zheng, O. F. Mohammed, Z. Chen, and O. M. Bakr, Shape control of metal halide perovskite single crystals: From bulk to nanoscale, Chem. Mater. **32**, 7602 (2020).

[35] Y. Xiong, W.-Y. Yi, G.-W. Yang, and Y.-H. Yang, Elongated hexagonal ZnO micro-fence optical resonator, Curr. Appl. Phys. **19**, 984 (2019).

[36] C. P. Dietrich, M. Lange, C. Sturm, R. Schmidt-Grund, and M. Grundmann, One-and two-dimensional cavity modes in ZnO microwires, New J. Phys. **13**, 103021 (2011).

[37] C. P. Dietrich, M. Lange, F. J. Klüpfel, H. von Wenckstern, R. Schmidt-Grund, and M. Grundmann, Strain distribution in bent ZnO microwires, Appl. Phys. Lett. **98**, 031105 (2011).

[38] Y. Zhu, Y. Zhou, M. I. B. Utama, M. de la Mata, Y. Zhao, Q. Zhang, B. Peng, C. Magen, J. Arbiol, and Q. Xiong, Solution phase van der Waals epitaxy of ZnO wire arrays, Nanoscale **5**, 7242 (2013).

[39] H. Dong, Y. Liu, S. Sun, J. Li, J. Zhan, Z. Chen, and L. Zhang, Geometry dependent evolution of the resonant mode in ZnO elongated hexagonal microcavity, Sci. Rep. **6**, 19273 (2016).

[40] M. Tang, Y.-D. Yang, H.-Z. Weng, J.-L. Xiao, and Y.-Z. Huang, Ray dynamics and wave chaos in circular-side polygonal microcavities, Phys. Rev. A **99**, 033814 (2019).

[41] A. J. Lichtenberg and M. A. Lieberman, *Regular and Stochastic Motion*, Applied Mathematical Sciences (Springer, New York, 1983), Vol. 38.

[42] S. Sottini, Geodesic optics, in *New Directions in Guided Wave and Coherent Optics*, edited by D. B. Ostrowsky and E. Spitz, NATO Science Series E, Vol. 78/79 (Springer, Dordrecht, 1984), pp. 545–575.

[43] M. Šarbort and T. Tyc, Spherical media and geodesic lenses in geometrical optics, J. Opt. **14**, 075705 (2012).

[44] L. Xu, X. Wang, T. Tyc, C. Sheng, S. Zhu, H. Liu, and H. Chen, Light rays and waves on geodesic lenses, Photonics Res. **7**, 1266 (2019).

[45] L. Xu, R. He, K. Yao, J. M. Chen, C. Sheng, Y. Chen, G. Cai, S. Zhu, H. Liu, and H. Chen, Conformal singularities and topological defects from inverse transformation optics, Phys. Rev. Appl. **11**, 034072 (2019).

[46] M. Hentschel and K. Richter, Quantum chaos in optical systems: The annular billiard, Phys. Rev. E **66**, 056207 (2002).

[47] J. Wiersig and M. Hentschel, Unidirectional light emission from high-Q modes in optical microcavities, Phys. Rev. A **73**, 031802(R) (2006).

[48] A. Bäcker and R. Schubert, Chaotic eigenfunctions in momentum space, J. Phys. A: Math. Gen. **32**, 4795 (1999).